

Research Article

<https://doi.org/10.1631/jzus.A2200235>



Examining the influence of the loading path on the cracking characteristics of a pre-fractured rock specimen with discrete element method simulation

Kang DUAN, Ri-hua JIANG, Xue-jian LI, Lu-chao WANG, Ze-ying YANG✉

School of Civil Engineering, Shandong University, Jinan 250061, China

Abstract: Damage in a rock mass is heavily dependent on the existence and growth of joints, which are also influenced by the complex stress states induced by human activities (e.g., tunneling and excavation). A proper representation of the loading path is essential for understanding the mechanical behaviors of rock masses. Based on the discrete element method (DEM), the influence of the loading path on the cracking process of a rock specimen containing an open flaw is examined. The effectiveness of the model is confirmed by comparing the simulation results under a uniaxial compression test to existing research findings, where wing crack initiates first and secondary cracks contribute to the failure of the specimen. Simulation results confirm that the cracking process is dependent upon both the confining pressure and the loading path. Under the axial loading test, a higher confining pressure suppresses the development of tensile wing cracks and forces the formation of secondary cracks in the form of shear bands perpendicular to the flaw. Increase of confining pressure also decreases the influence of the loading path on the cracking process. Reduction of confining pressure during an unloading test amplifies the concentration of tensile stress and ultimately promotes the appearance of a tensile splitting fracture at meso-scale. Confining pressure at the failure stage is well predicted by the Hoek-Brown failure criterion under quasi-static conditions.

Key words: Cracking process; Loading path; Fractured rock mass; Discrete element method (DEM); Local stress concentration


1 Introduction

Rock masses are the construction medium in many rock-related engineering applications such as tunnels, caverns, and rock slopes. One of the most prominent features of the rock mass is the presence of discontinuities, in terms of faults, joints, or other natural planes of weakness (Hoek and Brown, 1980; Barton and Quadros, 2015). These structures, originating either from rock genesis (e.g., joints) or from loading history (e.g., cracks) (Duriez et al., 2016), play a dominant role in controlling the deformability and damage of rock engineering structures as they may serve as the initiator of fracturing or the path of fracture propagation. Therefore, understanding the influences of such structures on the fracturing of rock mass is essential

for the explanation of rock damage phenomena, the development of measures to control rock failure, and the design of support in underground construction. Following previous studies (Bobet and Einstein, 1998; Wong and Einstein, 2009), the term “flaw” will be used here for pre-existing discontinuities.

Since completely reproducing the whole physical process experienced by the surrounding rock mass is still difficult, experiments have been performed on the brittle rock specimen (e.g., granite and marble) or rock-like material specimen (e.g., gypsum and photo elastic material) to study the propagation and coalescence of pre-existing flaws under tension and compression (Brace and Bombolakis, 1963; Lajtai, 1974; Bobet and Einstein, 1998; Li et al., 2005; Wong and Einstein, 2009; Yang and Jing, 2011; Yang et al., 2016). In these experiments, fracturing characteristics and dependence on flaw geometry and other conditions have been systematically investigated. It was found that cracking processes are greatly affected by the mechanical and geometrical characteristics of the

✉ Ze-ying YANG, yangzy@sdu.edu.cn

 Kang DUAN, <https://orcid.org/0000-0001-6803-4803>

Received Apr. 30, 2022; Revision accepted July 25, 2022;
Crosschecked Oct. 8, 2022; Online first Jan. 23, 2023

© Zhejiang University Press 2023

initial flaw (Duriez et al., 2016). In general, two major types of cracks, i.e., the wing crack and the secondary crack, have been observed in a rock specimen with a single pre-existing flaw subjected to uniaxial compression (Bobet, 2000). The fracturing responses became more complicated when the specimen was subjected to multiaxial loading (Bobet and Einstein, 1998). In the experimental studies, the mechanisms of cracking are deduced from the fracture modes recorded by a high-speed camera (Wong and Einstein, 2009), high-resolution scanning electron microscopes (Bobet and Einstein, 1998), and acoustic emission information (Li et al., 2005). Although considerable insights towards the source of microcracks and their growth in response to applied loads have been obtained, the micro mechanics of cracks and its interaction with local stress concentration are hard to acquire with these experimental approaches. Moreover, most of the previous studies were conducted under uniaxial or biaxial compression conditions, which deviate a lot from the loading path experienced by in-situ rock masses.

In general, the initial in-situ stresses (vertical stress and lateral confining pressures) increase gradually with the depth of the site. As illustrated in Fig. 1, the rock mass in a buried excavation (e.g., tunnel and underground excavation) and open excavation (e.g., open pit mining and high rock slope) experiences various loading paths with the reduction of confining pressure caused by excavation. For the former (Fig. 1a), the vertical stress increases continuously with the redistribution of stress around the openings, but for the latter (Fig. 1b), the vertical stress maintains a constant magnitude resulting from the overburden (Martin,

1997; Malmgren et al., 2007; Zhang et al., 2017, 2019). The influences of loading path on the cracking processes of fractured rock mass remain largely unclear.

So far, the mechanical behaviors of intact rocks subjected to confining pressure unloading have been studied through laboratory tests and numerical simulations (Cai and Kaiser, 2005; He et al., 2010; Li et al., 2018; Duan et al., 2019a). Most of this research has focused on the dynamic responses of brittle rock subjected to the sudden removing of lateral confinement with the aim of modeling the excavation-induced rock burst phenomena. Nevertheless, previous studies have confirmed that the mechanical behavior of hard rock under unloading is different from that under loading (Duan et al., 2019a). Therefore, more effort is necessary to investigate the cracking process of pre-fractured rock specimens subjected to loading paths which are closer to the ones experienced by surrounding rock in real engineering applications.

Theoretical analysis and numerical simulations have also been performed to elucidate the fracturing process in a pre-fractured rock specimen (Tapponnier and Brace, 1976; Tang and Kou, 1998; Zhang et al., 2018). Although the stress state in the pre-fractured specimen can be calculated by the Griffith theory (Griffith, 1921; Brace, 1960), the subsequent growing process cannot be predicted. Crack propagation has been modeled by the meshless methods such as the extended finite element method (XFEM) (Duriez et al., 2016). Continuum methods rely largely on the complicated constitutive model and do not easily describe the propagation of cracks (Cundall, 2001). In this respect, the discrete element method (DEM) is able to

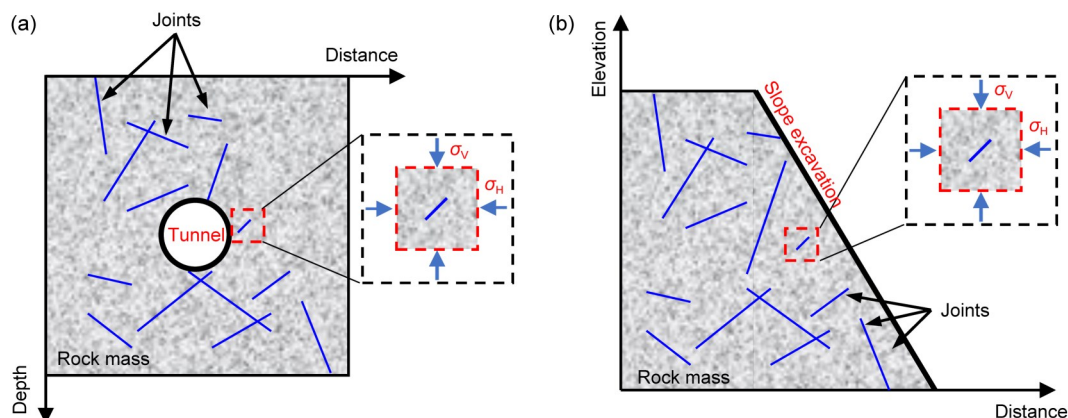


Fig. 1 Schematic diagrams showing the underground excavation (e.g., tunnel) (a) and the open excavation (e.g., slope) (b) in the fractured rock mass. σ_v is the vertical stress, and σ_h is the horizontal stress

simulate the actual dynamic fracturing behavior (Wong and Einstein, 2009). It has been extensively adopted in the modeling of the failure process of brittle rock and in the exploration of the micro-mechanisms underlying the fracturing process (Al-Busaidi et al., 2005; Duan and Kwok, 2016; Kwok et al., 2020). The propagation of fracture has also been modeled with DEM on both single and multiple pre-existing flaws (Wang and Mora, 2008; Zhang and Wong, 2013; Yang et al., 2014; Huang et al., 2019). Most recently, the cracking process under a confining pressure unloading condition has been simulated (Duan et al., 2019a). Given its ability to explicitly represent the fracturing process, DEM provides an ideal option for the examination of the fracturing characteristics of a pre-fractured rock specimen subjected to complicated loading paths.

With the DEM, we perform a comprehensive set of numerical tests on a specimen with a pre-existing open flaw dipping at 45° . The novelty of this study lies in a loading path purposely designed to mimic the stress states experienced by various engineering scenarios, including the axial loading test, the confining pressure unloading test, and the axial loading test accompanied by confining pressure unloading. Cracking phenomena and their dependence on the loading path and confining pressure are investigated. The micro-mechanism contributing to the fracturing process is also explored by examining the concentration of local stress and components of cracks.

2 Numerical methodology

2.1 Discrete element method

Simulations in this study are conducted with the particle flow code in two dimensions (PFC2D), which is a commercial software developed based on the DEM (Potyondy and Cundall, 2004; Itasca, 2008). The rock matrix is represented by the bonded particle model in which an assembly of rigid particles is bonded at their contacts (Fig. 2). The movement of each particle is described by Newton's second law while the interaction between the contacting pair of particles is controlled by the contact model which defines the force–deformation relationship. During the past two decades, various contact models have been developed to simulate the different aspects of rock behaviors (Potyondy and Cundall, 2004; Mas Ivars et al., 2008; Potyondy,

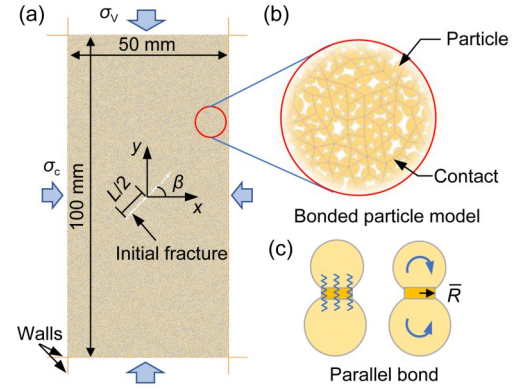


Fig. 2 Setup of the DEM model: (a) geometry of the rock specimen containing a pre-existing open flaw; (b) bonded particle model; (c) parallel bond. σ_c is the confining pressure, L is the length of the initial fracture, β is the dip of the initial fracture, and \bar{R} is the radius of the parallel bond

2012). The parallel bond model, which has been extensively adopted in the simulation of brittle rock failure characteristics, is selected in this study.

As shown in Fig. 2c, a parallel bond can be envisioned as a set of elastic springs uniformly distributed over a rectangular section with a thickness of 1. The relationship between the relative displacement and contact force of particles can be calculated by the linear contact model. Details of the corresponding constitutive equations can be found in references (Potyondy and Cundall, 2004; Itasca, 2008). Failure of the parallel bond depends on the maximum stress, either tensile or shear, acting on the periphery of the bond, which is calculated by:

$$\bar{\sigma}_{\max} = \frac{-\bar{F}_n}{A} + \frac{|\bar{M}_s| \bar{R}}{I}, \quad (1)$$

$$\bar{\tau}_{\max} = \frac{|\bar{F}_s|}{A} + \frac{|\bar{M}_n| \bar{R}}{J}, \quad (2)$$

where $\bar{\sigma}_{\max}$ is the maximum tensile stress; $\bar{\tau}_{\max}$ is the maximum shear stress; \bar{F}_n and \bar{F}_s are the normal force and shear force, respectively; \bar{M}_n and \bar{M}_s denote the moment in the normal and shear directions, respectively; A , I , and J are the area, moment of inertia, and planar moment of inertia of the parallel bond cross section, respectively.

The parallel bond breaks once $\bar{\sigma}_{\max}$ exceeds its tensile strength ($\bar{\sigma}_c$), or $\bar{\tau}_{\max}$ exceeds the shear strength ($\bar{\tau}_c$). In this way, the initiation, propagation, and coalescence of rock cracking can be explicitly simulated. Local bond breakages are denoted as micro-cracks in this

study. The bond breakage caused by tensile stress is recorded as one tensile micro-crack while the one induced by shear stress is taken as one shear micro-crack.

2.2 Setup of the numerical specimen

A rectangular model with a height of 100 mm and a width of 50 mm is constructed following the procedures recommended by Potyondy and Cundall (2004). The intact rock specimen consists of 20694 particles, with the size evenly distributed between 0.2 mm and 0.332 mm. The porosity of the numerical model is 15.3% while the coordination number is 4.07. To ensure that the model generated each time has the same particle distribution, a fixed random number needs to be set. Rock heterogeneity is mainly found in microstructure (mineral grain size) and micro-strength (bond strength between mineral grains) (Jiang et al., 2022). In the numerical rock specimen, heterogeneity of rock is introduced by assigning a wide particle size distribution and the bond strength follows a normal distribution. We modify the mean and variance of the normal distribution to control the heterogeneity of the micro contact strength.

In the DEM model, flaws can be represented either by inserting the smooth joint model (Duan et al., 2019b) or by deleting certain particles located in the flaw area. In this study, an open flaw is introduced in the center of the specimen by deleting particles located within the range of the flaw. As shown in Fig. 2a, all particles located in the central area of the specimen are deleted to mimic an open flaw. Since this study focuses on examining the influence of a loading path, we only consider the open flaw with an inclined dipping angle of 45°. Effects of other geometric and mechanical properties of the flaws (e.g., dipping angle, length, filling conditions, and roughness) remain to be explored in future studies. Another two parameters defining the

flaw geometry include the length and the aperture, which are set to be 20 mm and 1.2 mm, respectively. Altogether 56 particles are deleted corresponding roughly with two particles within the pre-existing flaw given the averaged particle diameter of 0.53 mm. DEM specimen setup parameters and pre-existing open flaw geometry are shown in Table 1.

Table 1 Setup of the DEM specimen and the geometry of the pre-existing open flaw

Parameter	Value
Specimen	
Width (mm)	50
Height (mm)	100
Number of particles	20694
Porosity (%)	15.3
Coordination number	4.07
Flaw	
Length of the flaw, L (mm)	20
Aperture of the flaw (mm)	1.2
Inclination angle (°)	45
Number of particles deleted	56

2.3 Loading path

Three loading paths are designed to reveal the cracking characteristics of the pre-fractured specimen. As illustrated in Fig. 3, all three paths share the same initial two stages. Both the axial stress and confining pressure are increased simultaneously to the pre-determined confining pressure level (stage I). After that, the confining pressure is kept constant while the axial stress is monotonically increased to the pre-designed axial stress magnitude (stage II). It should be emphasized that for the loading paths 2 and 3, under the same confining pressure (σ_3) conditions, the axial stress (σ_1) is loaded to 220, 250, and 280 MPa,

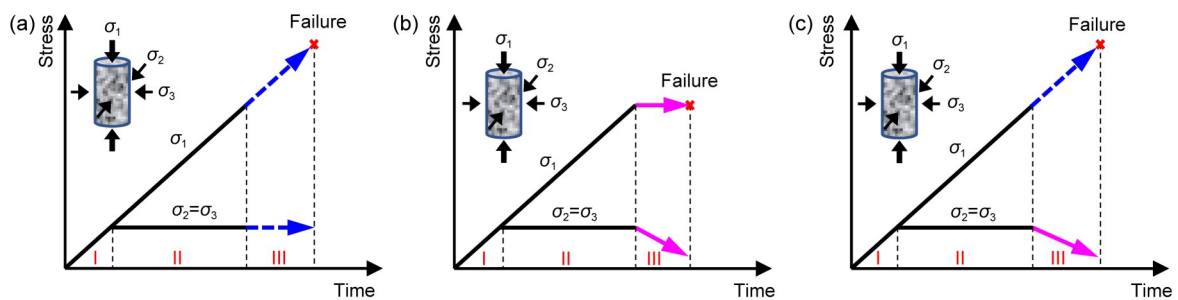


Fig. 3 Loading paths for the axial loading test (a), the confining pressure unloading test (b), and the axial loading test accompanied by the confining pressure unloading (c)

respectively. The last stages are different for the three loading paths:

1. Axial loading test (path 1): The confining pressure is maintained constant by adjusting the location of lateral walls with the servo control mechanisms while the top and bottom walls are moved towards each other until the failure of the specimen.

2. Confining pressure unloading test (path 2): The axial stress is maintained constant with the servo control mechanism while the confining pressure is reduced with a constant rate by moving the lateral walls away from each other.

3. Axial loading test accompanied by confining pressure unloading (path 3): The axial load is increased with a constant rate while the confining pressure is reduced with the same rate.

In our previous study, the influence of unloading rate on the failure behaviors of brittle rock was examined (Duan et al., 2019a). We adopted the unloading rate of 1.97×10^{-5} MPa/cycle, which belongs to the quasi-static regime. The axial stress and lateral stress acting on the walls are recorded. The axial strain is calculated based on the displacement of the top and bottom walls. All micro-cracks formed during the simulation are recorded.

3 Selection of micro-parameters and validation of the model

3.1 Selection of micro-parameters

It is well known that the micro-parameters of the bonded particle model are hard to measure directly by tests in the laboratory. Hence, an extensive calibration procedure, based on trial and error, is normally required to find the optimal set of parameters. The micro-parameters used in this study (Table 2) are calibrated to reproduce the mechanical properties of the Bukit Timah granite subjected to a triaxial compression test under the confining pressure of 20 MPa (Duan et al., 2019a). Comparison among the peak strength, elastic modulus, and Poisson's ratio obtained from the numerical simulation and the experiments on an intact specimen is provided in Table 3, in which a generally good agreement can be found. With these micro-parameters, virtual tests are performed on the specimen containing an open flaw subjected to the various loading paths discussed in Section 2.3.

Table 2 Micro-parameters calibrated to represent the Bukit Timah granite

Micro-parameter	Value	Micro-parameter	Value
R_{\min} (mm)	0.2	\bar{E}_c (GPa)	46.5
R_{\max}/R_{\min}	1.66	$\bar{\sigma}_c$ (MPa)	222.0±22.2
E_c (GPa)	46.5	$\bar{\tau}_c$ (MPa)	222.0±22.2
ρ (kg/m ³)	3169	\bar{k}_n/\bar{k}_s	1.86
μ	0.5	λ	1
k_n/k_s	1.86		

R_{\min} is the minimum radius of particles; R_{\max}/R_{\min} is the ratio between the maximum and minimum radii; E_c is Young's modulus of particles; ρ is the particle density; μ is the friction coefficient between particles; k_n/k_s is the ratio of the normal to shear stiffness of particles; \bar{E}_c is Young's modulus of parallel bonds; \bar{k}_n/\bar{k}_s is the ratio of normal to shear stiffness of the parallel bonds; λ is the multiplier used to set the radii of parallel bonds

Table 3 Comparison between the experimental and numerical results on Bukit Timah granite under the confining pressure of 20 MPa (Duan et al., 2019b)

Result	Peak strength (MPa)	Elastic modulus (GPa)	Poisson's ratio
DEM simulation	373.4	64.5	0.186
Experimental	373.1	64.8	0.184

3.2 Validation of the model

One of the prerequisites of using DEM to investigate rock behaviors is to validate its capability and accuracy by comparing the simulation results with results from experiments or from analytical solutions. We compare the cracking process of the pre-fractured specimen subjected to a uniaxial compression test with experimental findings from the literature.

The stress-strain curve in Fig. 4 generally follows the linear elastic response with no cracks at the initial stage. Micro-cracks start to emerge after the vertical strain exceeds 0.15% and increase in a slow and stable way until the axial strain reaches 0.30% (stage A in Fig. 4). At this stage, two wing cracks initiate from the tips of the flaw and propagate along an orientation of almost 90° with respect to the flaw (Fig. 5a), which is consistent with the general observations that wing cracks appear first in terms of tensile cracks at the tip of a pre-existing flaw (Bobet and Einstein, 1998) (Fig. 5f). The wing cracks grow in a stable manner, as confirmed by previous study (Bobet and Einstein, 1998). Thereafter, the stress-strain curve deviates from linear elastic and the number of micro-cracks increases

quickly. The accumulations of micro-cracks apart from the wing cracks can be observed in Figs. 5b and 5c, in front of the upper tip and on the opposite of the wing crack at the lower tip. After the peak stress (stage D), the vertical stress soon drops and is accompanied by a

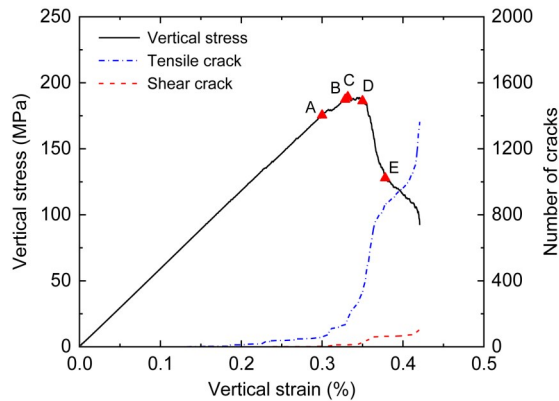


Fig. 4 Variation of the vertical stress and the number of micro-cracks versus the vertical strain obtained from the uniaxial compression test on the pre-fractured specimen

dramatic increase in the number of micro-cracks. The growth path of the wing cracks is curvilinear and along the maximum principal stress direction, consistent with the phenomenon observed from Brace and Bombolakis (1963) (Fig. 5g). The accumulation of micro-cracks along the lower secondary crack develops into one major shear fracture crossing the specimen with the orientation almost perpendicular to the initial flaw (Fig. 5e). This phenomenon is also in line with previous findings that the shear fracture causes the failure of the pre-fractured specimen. Several meso tensile fractures branch from the major fracture and grow vertically along the major principal stress orientation. The present crack growth trajectories agree well with experimental observations (Bobet, 2000; Wong and Einstein, 2009) and simulation results obtained from other approaches (Wang et al., 2017), confirming that the DEM model is capable of representing the loading-induced cracking in a pre-fractured rock specimen.

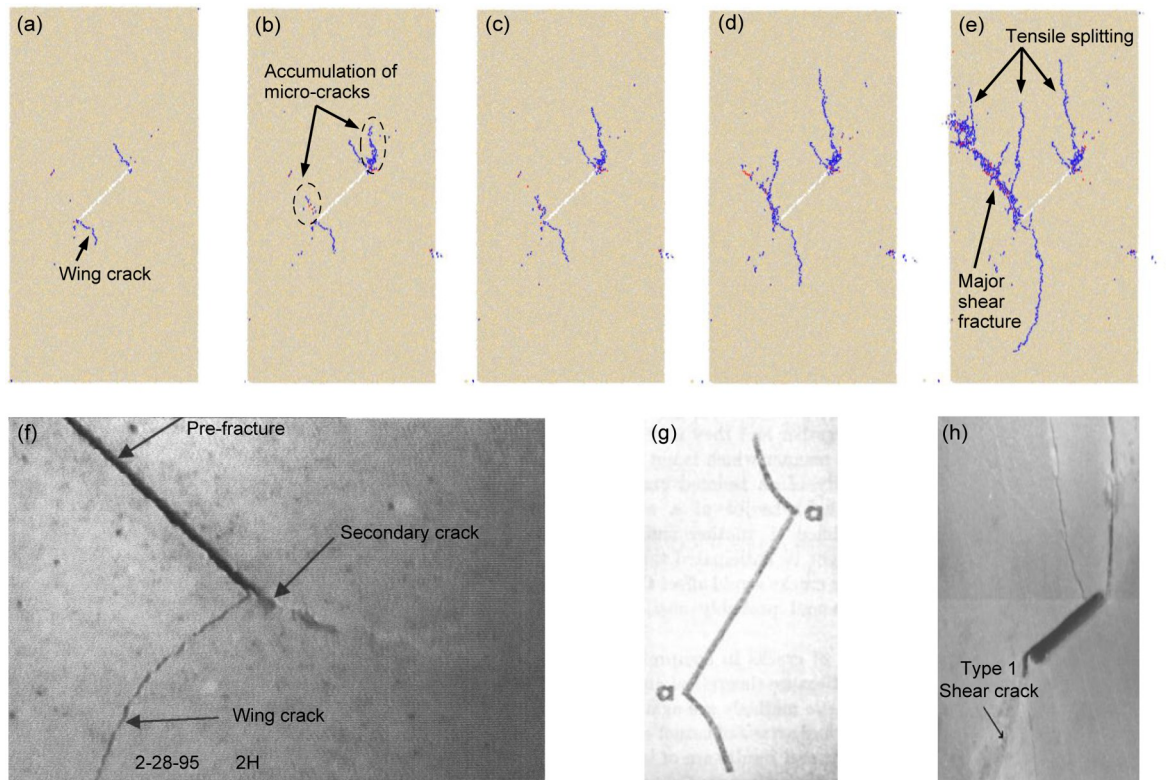


Fig. 5 Temporal-spatial evolution of cracks under the uniaxial compression test (a–e), and the experimental observations (f–h). Tensile cracks are represented by blue short lines and shear cracks are represented by red short lines. Corresponding stages A–E are marked in Fig. 4. Fig. 5f is reprinted from (Bobet and Einstein, 1998), Copyright 1998, with permission from Elsevier; Fig. 5g is reprinted from (Brace and Bombolakis, 1963), Copyright 1963, with permission from American Geophysical Union; Fig. 5h is reprinted from (Wong and Einstein, 2009), Copyright 2009, with permission from Elsevier. References to color refer to the online version of this figure

4 Simulation results

We performed systematic simulations on the pre-fractured specimen subjected to the axial loading, confining pressure unloading, and the axial loading accompanied by confining pressure unloading tests following the loading paths discussed in Section 2.3. The vertical stress, confining pressure, axial strain, and spatial-temporal evolution of micro-cracks are discussed in this section as the characteristics of deformation evolution, displacement variation, and cracking process are necessary precursors of numerous phenomena and disasters in deep rock engineering.

4.1 Axial loading test

It is well known that the strength, cracking process, and macroscopic failure pattern depend largely on the magnitude of the confining pressure (Martin and Chandler, 1994; Martin, 1997; Duan et al., 2015). We conducted axial loading tests with the confining pressure $\sigma_c=10, 20$, and 30 MPa, to evaluate its influence on the cracking of a pre-fractured specimen. Based on

the stress–strain history and number of micro-cracks (Fig. 6), the cracking process can be generally divided into three stages. None micro-crack forms at the beginning of the linear elastic stage. When the axial strain exceeds 0.2%, micro-cracks start to initiate in terms of tensile failure of parallel bond. The deformability gradually enters the non-linear stage with the appearance of micro-cracks. The number of micro-cracks increases dramatically at the post-peak stage.

Fig. 7 shows that the influences of confining pressure on the mechanical properties of the pre-fractured specimen are generally consistent with those from the intact specimens (Duan et al., 2017). Both the peak strength and the elastic modulus increase with the confining pressure. The pre-existing flaw reduces the peak strength to 58% of the intact specimen when $\sigma_c=0$ MPa while this ratio monotonically increases to around 80% when $\sigma_c=30$ MPa, indicating that higher confining pressure decreases the influence of flaw on the strength of fractured rock. The elastic moduli of both the intact specimen and the fractured specimen slightly increase with higher confining pressure. The two curves stay

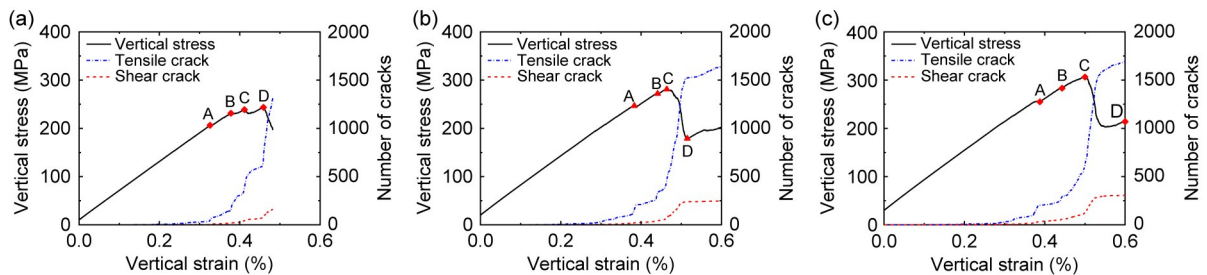


Fig. 6 Stress–strain curve and the number of micro-cracks obtained from the triaxial compression tests on the specimen under the confining pressure of 10 MPa (a), 20 MPa (b), and 30 MPa (c), respectively

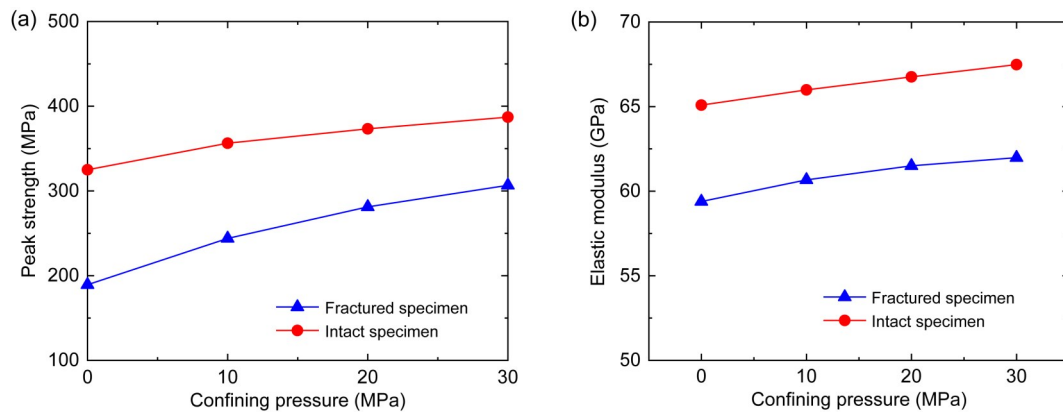


Fig. 7 Comparison between the peak strength (a) and the elastic modulus (b) obtained from the intact specimen and the pre-fractured specimen when subjected to uniaxial compression test and the triaxial compression test with the confining pressure varying from 10 to 30 MPa

almost parallel with each other with the reduction ratio of the fractured specimen being around 60%. These results suggest that the effect of confining pressure on the deformability is less significant than its effect on the strength of the pre-fractured specimen.

The spatial-temporal evolution of micro-cracks in Fig. 8 demonstrates apparent distinct cracking patterns under different confining pressures. Wing cracks appear first in the test with $\sigma_c=10$ MPa. As the vertical stress is increased, more cracks emanate ahead of the lower tip and eventually lead to the major shear fracture in a plane roughly coplanar with the flaw (Fig. 8a).

With higher confining pressure (Figs. 8b and 8c), cracking is only produced through secondary cracks from the tips of the flaw. These cracks propagate in a stable manner along the orientations perpendicular to the flaw. Several meso-fractures appear in front of the lower tip but the specimen fails in terms of two major shear bands along the anti-wing crack orientation. This phenomenon has also been recognized by many researchers as shear cracks (Bobet, 2000). The transition of cracking patterns subjected to different confining pressures was also pointed out by Bobet and Einstein (1998).

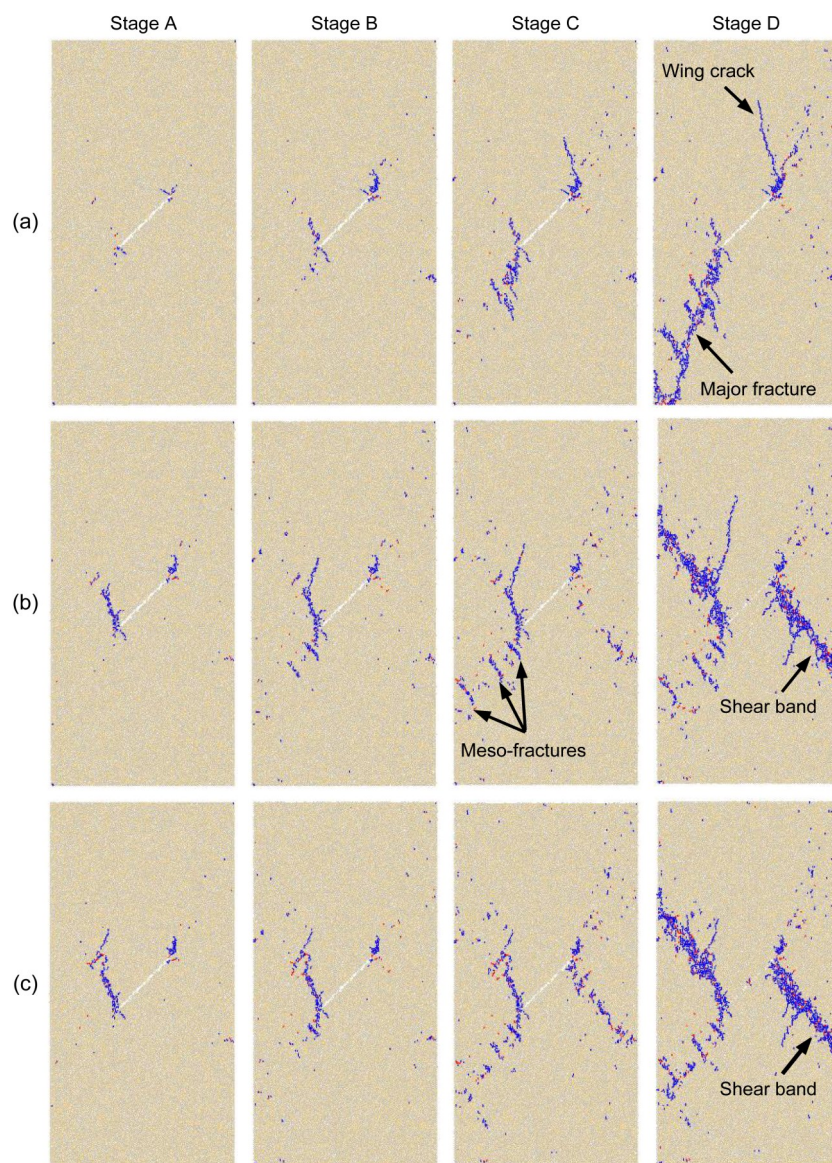


Fig. 8 Temporal-spatial evolution of micro-cracks from the axial loading tests: (a) $\sigma_c=10$ MPa; (b) $\sigma_c=20$ MPa; (c) $\sigma_c=30$ MPa. Tensile cracks are represented by blue lines and shear cracks are represented by red lines. The stages are marked in Fig. 6. References to color refer to the online version of this figure

4.2 Confining pressure unloading test

Confining pressure unloading tests were conducted under the initial confining pressure $\sigma_{c0}=30$ MPa. The axial stress was increased to 220, 250, and 280 MPa, respectively, and then kept constant during the unloading of the confining pressure. During the test, the two lateral walls are moved away with the servo control mechanism to meet the following relationship:

$$\sigma_{ct} = \sigma_{c0} - \Delta\sigma \times t_{cyc}, \quad (3)$$

where σ_{ct} is the confining pressure after the unloading test running for t_{cyc} cycles, and $\Delta\sigma$ denotes the unloading rate.

The histories of stresses, axial strain, and number of micro-cracks in Fig. 9 can be generally divided into three stages. At the first stage (before stage A), the axial stress is increased to the predetermined level accompanied by the growth of vertical strain following the linear elastic deformation. With unloading (after stage A), the vertical strain slightly increases following the Poisson effect caused by the reduction of lateral confinement. The number of micro-cracks increases in a slow and stable manner. Finally, the specimen fails when the confining pressure is reduced to 5.89, 14.78, and 22.16 MPa, respectively. Fast growth of the axial

strain indicates the collapse of the specimen accompanied by the formation of a large number of micro-cracks in a short time. The fluctuation of the axial stress history suggests that the specimen loses load-carrying capacity and the servo control mechanism fails to maintain a constant axial stress.

The spatial-temporal evolutions of micro-cracks in Fig. 10 confirm that the cracking characteristics under confining pressure unloading differ from those induced by axial loading (Fig. 8). Before the start of unloading (the left column), the secondary cracks already emerge along the anti-wing crack orientation (Figs. 10b and 10c). With the ongoing of the unloading test, the wing crack initiates from the flaw tips in the specimen under the initial axial stress of 220 MPa. Failure of the specimen is accompanied by the appearance of several meso-fractures propagating sub vertically (stage C in Fig. 10a). These fractures coalesce into a wide fractured zone ahead of the lower tip while a major fracture appears from the upper tip of the flaw to the right top corner of the specimen. The specimen subjected to an initial axial stress of 250 MPa also fails by the major shear fracture and the fractured zone but the secondary cracks extend in a more restrained and diffuse manner compared to the meso-fractures in Fig. 10a. Under the highest axial stress (280 MPa), the specimen fails in terms of two

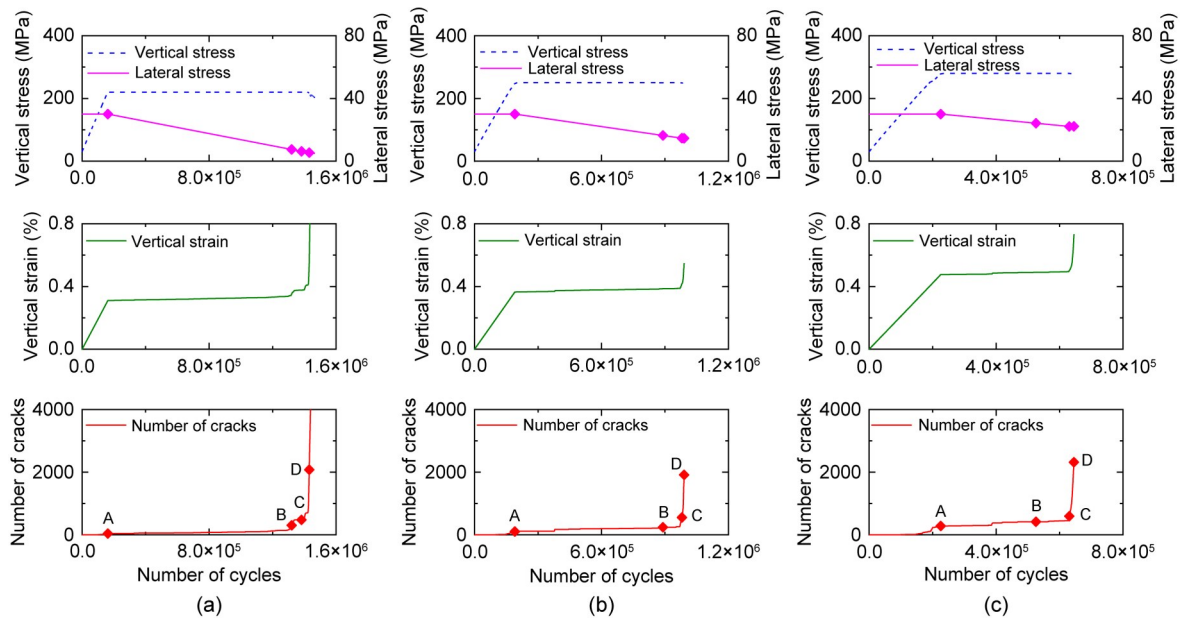


Fig. 9 Variation of the vertical stress, vertical strain, and number of micro-cracks versus the number of calculation cycles from the confining pressure unloading tests: (a) $\sigma_{c0}=30$ MPa, $\sigma_v=220$ MPa; (b) $\sigma_{c0}=30$ MPa, $\sigma_v=250$ MPa; (c) $\sigma_{c0}=30$ MPa, $\sigma_v=280$ MPa

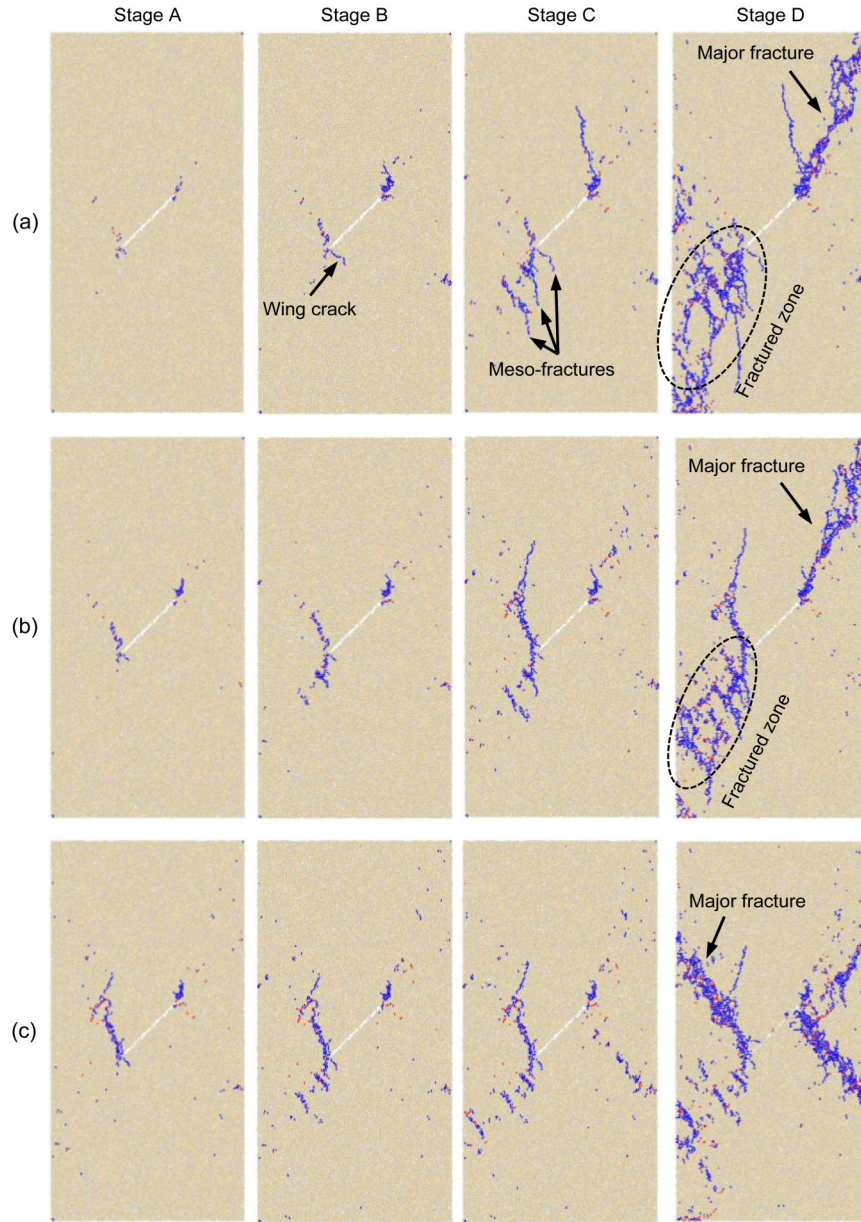


Fig. 10 Temporal-spatial evolution of micro-cracks from the confining pressure unloading tests: (a) $\sigma_c=30$ MPa, $\sigma_v=220$ MPa; (b) $\sigma_c=30$ MPa, $\sigma_v=250$ MPa; (c) $\sigma_c=30$ MPa, $\sigma_v=280$ MPa. Tensile cracks are represented by blue lines and shear cracks are represented by red lines. The stages are marked in Fig. 9. References to color refer to the online version of this figure

shear bands perpendicular to the initial flaw (Fig. 10c), which is similar to the ones subjected to axial loading when $\sigma_c=10$ and 20 MPa, suggesting that the influence of the loading path becomes less significant under higher confining pressures.

4.3 Axial loading test accompanied by confining pressure unloading

For the axial loading test accompanied by confining pressure unloading, in addition to the unloading

of confining pressure described by Eq. (3), the axial stress also increases following:

$$\sigma_{v_t} = \sigma_{v_0} + \Delta\sigma \times t_{\text{cyc}}, \quad (4)$$

where σ_{v_t} is the axial stress after the test has run for t_{cyc} cycles, and σ_{v_0} is the initial axial stress.

As shown in Fig. 11, the evolution of stresses, axial strain, and the number of micro-cracks is similar to those of the confining pressure unloading tests,

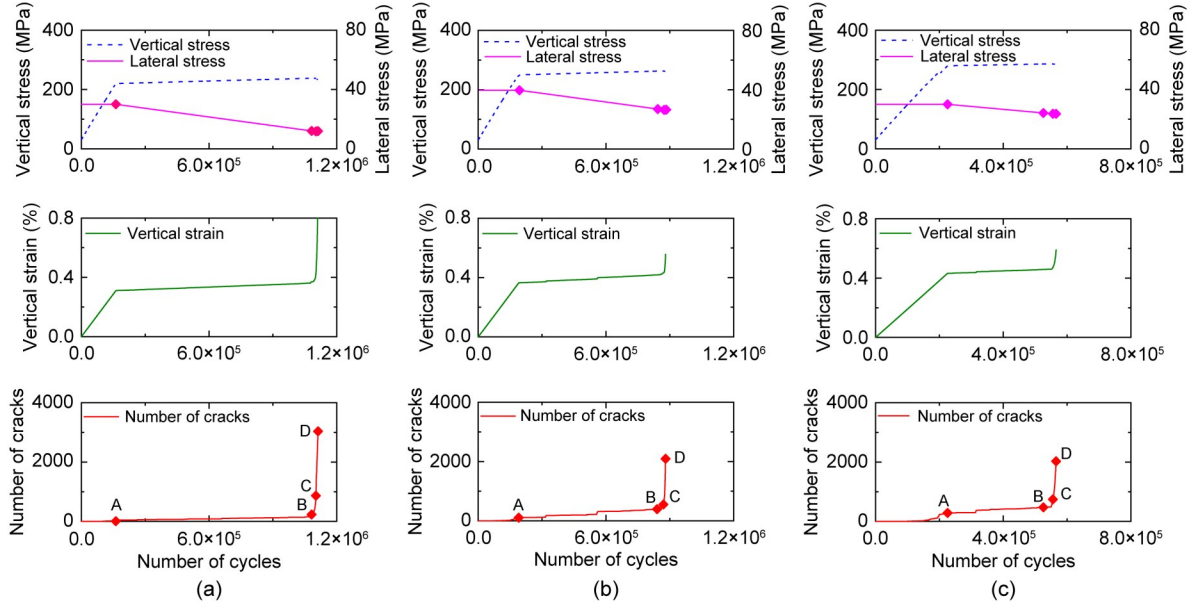


Fig. 11 Variation of the vertical stress, vertical strain, and number of micro-cracks versus the number of calculation cycles from the axial loading test accompanied by confining pressure unloading: (a) $\sigma_c=30$ MPa, $\sigma_v=220$ MPa; (b) $\sigma_c=30$ MPa, $\sigma_v=250$ MPa; (c) $\sigma_c=30$ MPa, $\sigma_v=280$ MPa

despite the duration of the tests and the magnitude of the confining pressure at the failure stage. When the specimen collapses, the corresponding confining pressures are 11.88, 16.82, and 23.67 MPa, respectively. Obviously, the confining pressure at failure stage is higher than that in a pure confining pressure unloading test, implying that the surrounding rock in the underground excavation fails more easily than that in the open excavation under the same in-situ stress conditions. Note that the increase of axial strain from stage A to stage B is more significant than that in Fig. 9 as the deformation is caused by not only the confining pressure unloading as in Fig. 9 but also the axial loading.

Slight differences exist between the evolution of fractures under this loading path and Fig. 10. Wing crack and tensile splitting are less apparent for the specimen under $\sigma_{v0}=220$ MPa (Fig. 12a). In addition to the appearance of quasi-coplanar secondary fractures which propagate in rough trajectories and along the flaw direction (Fig. 12b), the concentration of micro-cracks perpendicular to the flaw can be noted at stage D, suggesting that the failure pattern shares the characteristics of the axial loading test (Fig. 8b) and the confining pressure unloading test (Fig. 10b). When $\sigma_{v0}=280$ MPa, an approximately X-shaped fracture forms after the failure of the specimen with two

major fractures perpendicular to the flaw orientation (Fig. 12c).

4.4 Evolution of local stresses

The DEM model can yield information regarding the equilibrium local stress states, which can be estimated by the average stress within a certain measurement region. We installed a set of measurement circles evenly distributed in the horizontal and vertical directions with a space of 1 mm. The diameter of the circles was 2 mm. Stress states measured by these circles (the principal stress in x direction σ_{xx} , the principal stress in y direction σ_{yy} , and the shear stress σ_{xy}) can be converted into the major principal stress states (the maximum principal stress σ_{\max} and the minimum principal stress σ_{\min}) as follows:

$$\sigma_{\max} = \frac{\sigma_{xx} + \sigma_{yy}}{2} + \sqrt{\left(\frac{\sigma_{xx} - \sigma_{yy}}{2}\right)^2 + \sigma_{xy}^2}, \quad (5)$$

$$\sigma_{\min} = \frac{\sigma_{xx} + \sigma_{yy}}{2} - \sqrt{\left(\frac{\sigma_{xx} - \sigma_{yy}}{2}\right)^2 + \sigma_{xy}^2}. \quad (6)$$

In this section, we examine the evolution of σ_{\max} and σ_{xy} as they dominate the occurrence of tensile and shear fractures. Local concentrations of tensile stress and high shear stress around the pre-existing flaw and

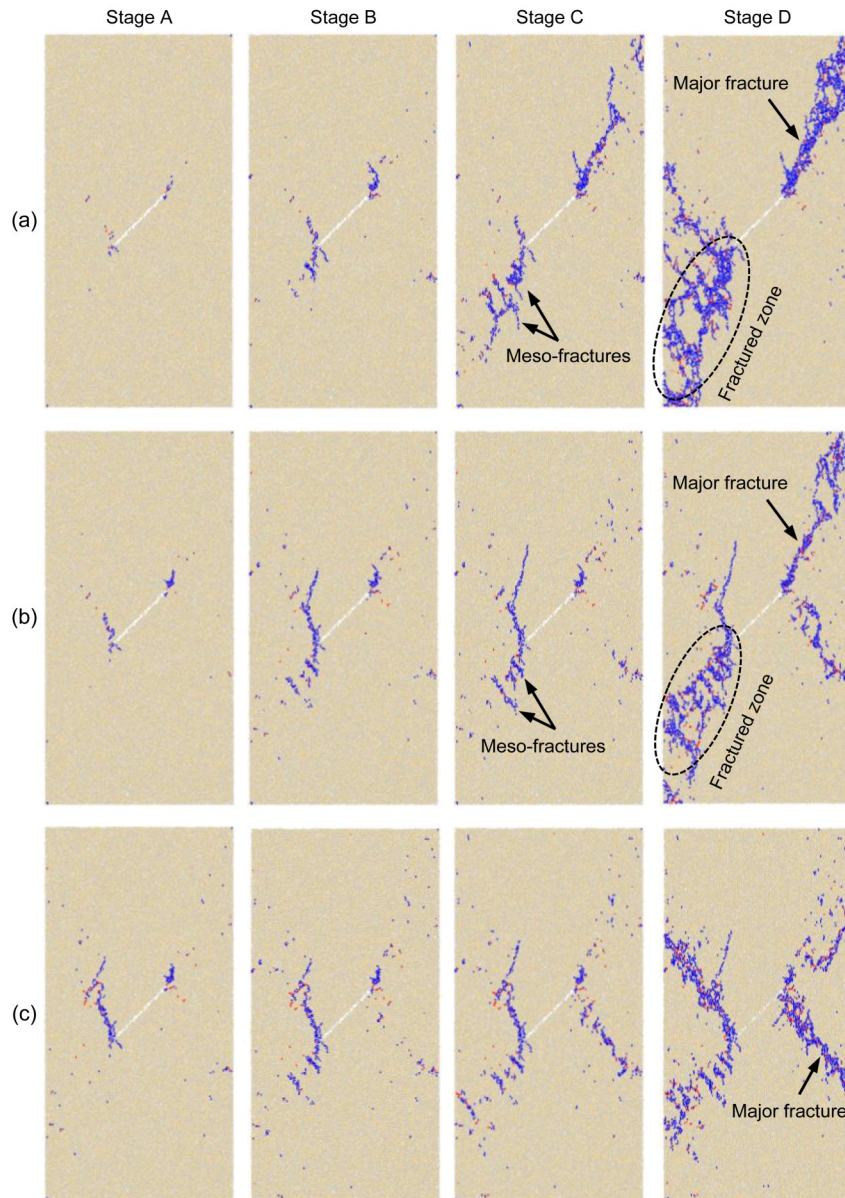


Fig. 12 Temporal-spatial evolution of the micro-cracks from the axial loading test accompanied by the confining pressure unloading: (a) $\sigma_c=30$ MPa, $\sigma_v=220$ MPa; (b) $\sigma_c=30$ MPa, $\sigma_v=250$ MPa; (c) $\sigma_c=30$ MPa, $\sigma_v=280$ MPa. Tensile micro-cracks are represented by blue short lines and shear micro-cracks are represented by red short lines. The stages are marked in Fig. 11. References to color refer to the online version of this figure

cracks can be identified from Figs. 13–15. In general, applied stresses are locally altered by the flaw, and become tensile at certain points ahead of the cracks, even when the applied stress is wholly compressive. This phenomenon is in accordance with the analytical solution results of Brace and Bombolakis (1963). Different from the maximum principal stress, the high shear stress mainly concentrates in four regions, i.e., two regions above the tips and two below the tips. These discrepancies contribute to the formation of

different cracking characteristics, either wing crack or secondary crack.

Concentration of the local stresses is in accordance with the cracking patterns discussed in Figs. 8 and 10. Before the unloading tests, high tensile stress appears in front of the initial cracks and shear stress displays centrosymmetric concentration with respect to the center of the flaw. The magnitude of confining pressure and the loading path lead to the distinct evolution of local stress. Concentration of tensile stress

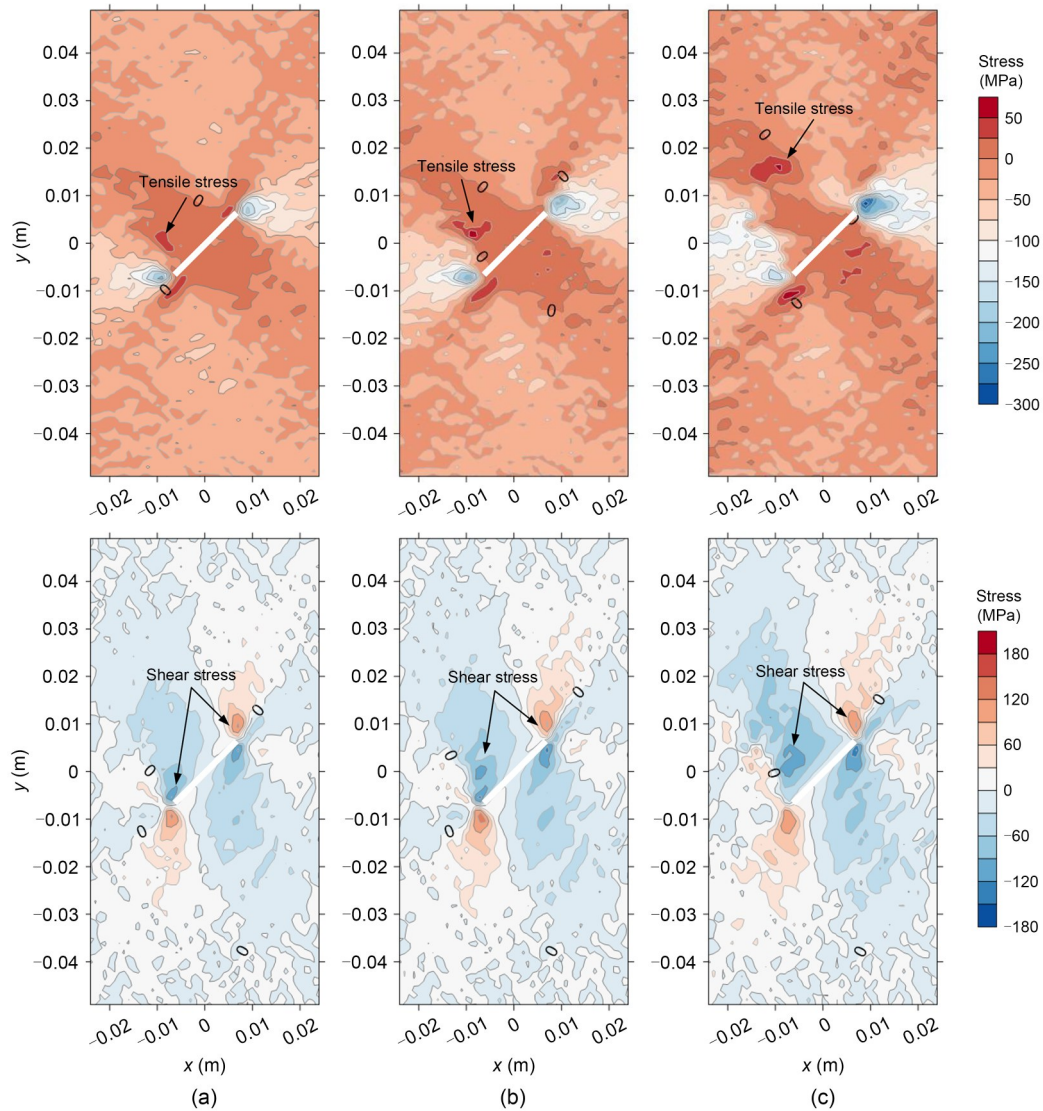


Fig. 13 Contours of the major principal stress (top column) and shear stress (bottom column) obtained from the specimens before unloading test: (a) $\sigma_c=30$ MPa, $\sigma_v=220$ MPa; (b) $\sigma_c=30$ MPa, $\sigma_v=250$ MPa; (c) $\sigma_c=30$ MPa, $\sigma_v=280$ MPa. Positive magnitude of the major principal stress indicates the tensile stress

becomes less significant with higher confining pressure (the top row in Figs. 14 and 15), indicating that higher confining pressure suppresses the occurrence of loading-induced tensile cracks, and, on the other hand, leads to the local concentration of high shear stress. Cracking behavior is dominated by the local stress state and the material properties. Tensile splitting fracture grows at the point with the maximum tensile stress and subsequently results in branch cracks. More sites under tension can be noted in the specimen subjected to confining pressure unloading (Fig. 15) than those in the one subjected to axial loading (Fig. 14), suggesting that the reduction of lateral confinement promotes

the formation of tensile splitting fractures. This is also supported by the meso-fractures in Fig. 10, especially when the initial confining pressure is low.

Components of micro-cracks formed between stages A and C are summarized in Fig. 16. It is clear that the tensile cracks take a major role in controlling the failure of the specimen, which is also confirmed in Figs. 8, 10, and 12. Tensile cracks take more than 80% for all the cases considered in Fig. 16. Moreover, the loading path also alters the mechanism of micro-cracks, which ultimately contributes to the macroscopic fracturing characteristics. The largest proportion of tensile cracks is obtained from the confining pressure

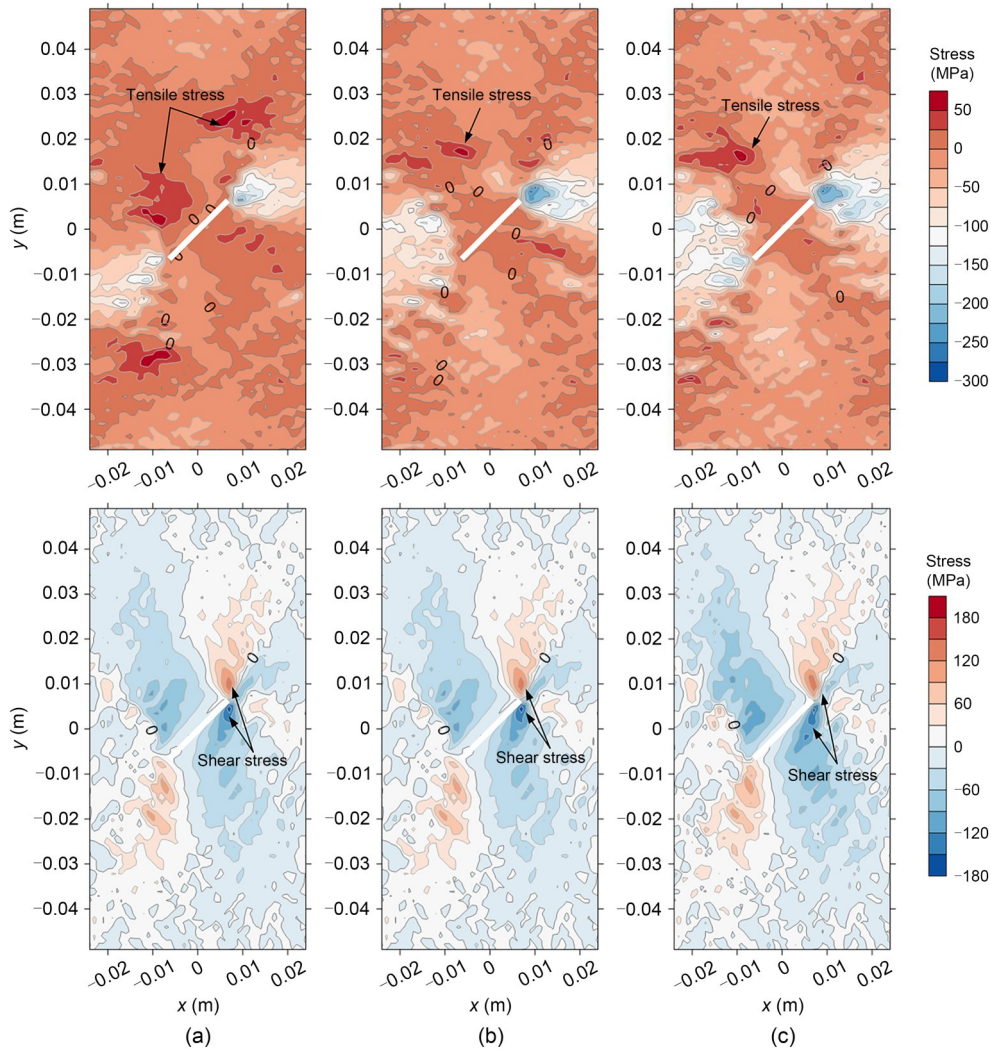


Fig. 14 Contours of the major principal stress (top column) and shear stress (bottom column) obtained from the axial loading tests conducted to stage C: (a) $\sigma_c=10$ MPa; (b) $\sigma_c=20$ MPa; (c) $\sigma_c=30$ MPa. Corresponding stages can be found in Fig. 6

unloading test while the smallest proportion is from the axial loading test. This phenomenon also supports the conclusion that a reduction of lateral confinement promotes the formation of tensile splitting fractures.

5 Discussion

The variation of peak strength obtained from the pre-fractured specimen displayed in Fig. 7a (the line with triangle) can be described by the Hoek-Brown failure criterion (Hoek and Brown, 1997) as:

$$\sigma_1 = \sigma_3 + \sigma_c \left(m_i \frac{\sigma_3}{\sigma_c} + 1 \right)^{\frac{1}{2}}, \quad (7)$$

where σ_c is the uniaxial compression strength of the pre-fractured specimen, and m_i is a material constant. Curve fitting results provide the parameters as follows:

$$\sigma_1 = \sigma_3 + 189.33 \times \left(7.88 \times \frac{\sigma_3}{189.33} + 1 \right)^{\frac{1}{2}}, \quad R^2 = 0.98. \quad (8)$$

Based on this failure criterion, confining pressure at the failure stage for the confining pressure unloading test and the axial loading test accompanied by confining pressure unloading can be estimated for a given initial axial stress and confining pressure. As compared in Fig. 17, the confining pressures at failure stage predicted by the failure criterion agree well with those

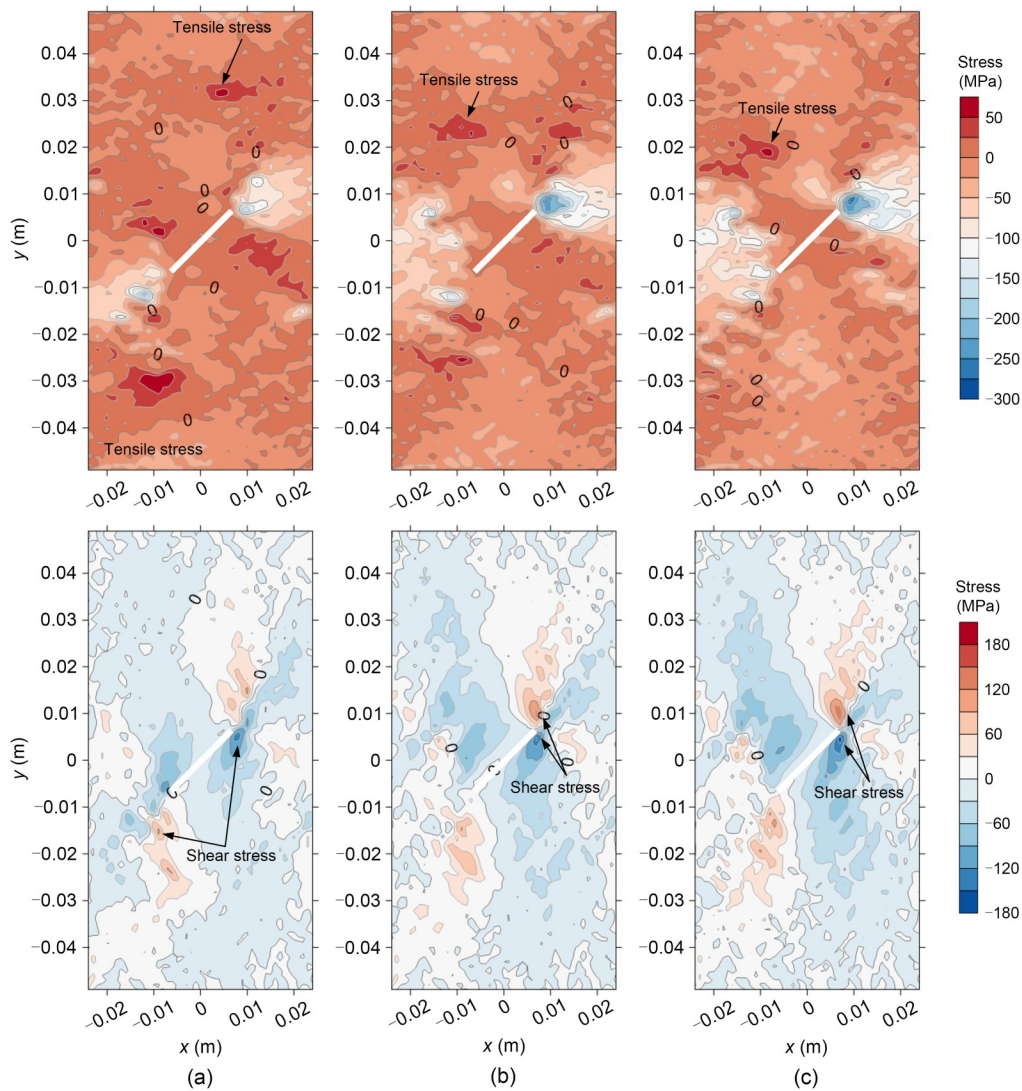


Fig. 15 Contours of the major principal stress (top column) and shear stress (bottom column) obtained from the confining pressure unloading tests conducted to stage C: (a) $\sigma_c=30$ MPa, $\sigma_v=220$ MPa; (b) $\sigma_c=30$ MPa, $\sigma_v=250$ MPa; (c) $\sigma_c=30$ MPa, $\sigma_v=280$ MPa. Corresponding stages can be found in Fig. 9

obtained from DEM simulations, suggesting that the failure responses of the pre-fractured specimen under complicated loading paths can be well captured by the failure criterion established on the quasi-static condition. The engineering implication of this result lies in the applicability of the Hoek-Brown failure criterion for the excavation-induced unloading under a high-stress condition subjected to a quasi-static process. Nonetheless, many studies have confirmed that the failure characteristic of brittle rocks is rate dependent (He et al., 2010; Duan et al., 2019a). Our previous study also revealed that the unloading rate plays an important role in the failure strength for the intact

rock (Duan et al., 2019a). Therefore, it is still necessary to investigate the fracturing process of the pre-fractured specimen subjected to fast confining pressure unloading to clarify the possible competition between the ejection from the lateral surface and the cracking around flaws.

The current study focuses on the influence of the loading path on the cracking characteristics with the consideration of the specimen containing a single flaw inclined at 45° . Previous studies have found that the location of the wing crack initiation depends on the inclination of the pre-existing flaw towards the direction of the major principal stress (Park and Bobet,

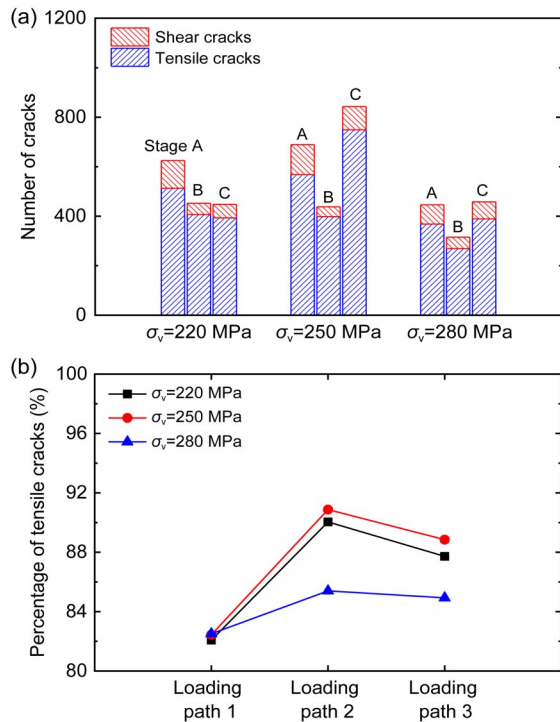


Fig. 16 Components of micro-cracks formed from the application of initial axial stress (stage A) to the failure stage (stage C) (a), and the percentage of tensile cracks (b), ($\sigma_c = 30$ MPa)

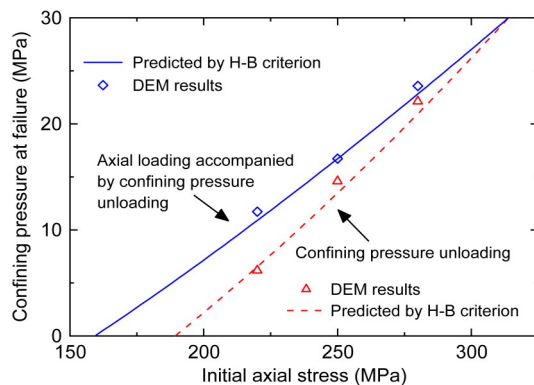


Fig. 17 Comparison between the confining pressures at failure stage predicted by the Hoek-Brown (H-B) failure criterion and those obtained from the DEM simulations under the initial confining pressure of 30 MPa

2009; Duriez et al., 2016). Other possible factors, including the geometry of flaws, filling conditions, and the magnitude of intermediate principal stress, have been confirmed as playing important roles in cracking subjected to axial loading tests. Therefore, the multiple-flaw system, considering the various dimensions, multiple flaws, and the unloading rate related to the excavation method, is worth further studying with the aim

of evaluating the influence of the geometry of flaws and the fracture coalescence during their propagation.

6 Conclusions

DEM simulations are conducted to evaluate the influences of the loading path on the cracking process of a pre-fractured rock specimen with three loading paths purposely designed to mimic the stress conditions experienced in various engineering scenarios. Under a uniaxial compression test, wing cracks initiate first from the tips of the flaw while secondary cracks in terms of shear fracture contribute to the failure of the specimen. The entire process agrees well with the findings from previous studies and thus confirms the capability of the model.

The trajectories and growth path of cracks depend on the confining pressure and loading path. Under the axial loading test, a higher confining pressure suppresses the formation of tensile fractures along the major principal stress orientation and leads to the appearance of a major shear band perpendicular to the pre-existing flaw. Confining pressure unloading promotes the formation of meso tensile splitting fractures compared with the axial loading test. The influence of the loading path on the cracking process declines with the increase of confining pressure.

The failure stage can be predicted by the Hoek-Brown failure criterion for the quasi-static process. The formation of different cracking characteristics is dominated by the local stress concentration. Higher confining pressure leads to the local concentration of high shear stress. The reduction of confining pressure amplifies the concentration of tensile stress and ultimately promotes the formation of tensile splitting fractures at the meso-scale.

Acknowledgments

This work is supported by the Shandong Provincial Natural Science Foundation of China (No. ZR2020YQ44) and the National Natural Science Foundation of China (No. 51909138).

Author contributions

Kang DUAN designed the research. Xue-jian LI and Lu-chao WANG processed the corresponding data. Kang DUAN wrote the first draft of the manuscript. Ze-ying YANG helped to organize the manuscript. Kang DUAN and Ri-hua JIANG revised and edited the final version.

Conflict of interest

Kang DUAN, Ri-hua JIANG, Xue-jian LI, Lu-chao WANG, and Ze-ying YANG declare that they have no conflict of interest.

References

- Al-Busaidi A, Hazzard JF, Young RP, 2005. Distinct element modeling of hydraulically fractured Lac du Bonnet granite. *Journal of Geophysical Research: Solid Earth*, 110(B6): B06302.
<https://doi.org/10.1029/2004JB003297>
- Barton N, Quadros E, 2015. Anisotropy is everywhere, to see, to measure, and to model. *Rock Mechanics and Rock Engineering*, 48(4):1323-1339.
<https://doi.org/10.1007/s00603-014-0632-7>
- Bobet A, 2000. The initiation of secondary cracks in compression. *Engineering Fracture Mechanics*, 66(2):187-219.
[https://doi.org/10.1016/S0013-7944\(00\)00009-6](https://doi.org/10.1016/S0013-7944(00)00009-6)
- Bobet A, Einstein HH, 1998. Fracture coalescence in rock-type materials under uniaxial and biaxial compression. *International Journal of Rock Mechanics and Mining Sciences*, 35(7):863-888.
[https://doi.org/10.1016/S0148-9062\(98\)00005-9](https://doi.org/10.1016/S0148-9062(98)00005-9)
- Brace WF, 1960. An extension of the Griffith theory of fracture to rocks. *Journal of Geophysical Research*, 65(10): 3477-3480.
<https://doi.org/10.1029/JZ065i010p03477>
- Brace WF, Bombolakis EG, 1963. A note on brittle crack growth in compression. *Journal of Geophysical Research*, 68(12):3709-3713.
<https://doi.org/10.1029/JZ068i012p03709>
- Cai M, Kaiser PK, 2005. Assessment of excavation damaged zone using a micromechanics model. *Tunnelling and Underground Space Technology*, 20(4):301-310.
<https://doi.org/10.1016/j.tust.2004.12.002>
- Cundall PA, 2001. A discontinuous future for numerical modelling in geomechanics? *Proceedings of the Institution of Civil Engineers-Geotechnical Engineering*, 149(1):41-47.
<https://doi.org/10.1680/geng.2001.149.1.41>
- Duan K, Kwok CY, 2016. Evolution of stress-induced borehole breakout in inherently anisotropic rock: insights from discrete element modeling. *Journal of Geophysical Research: Solid Earth*, 121(4):2361-2381.
<https://doi.org/10.1002/2015JB012676>
- Duan K, Kwok CY, Tham LG, 2015. Micromechanical analysis of the failure process of brittle rock. *International Journal for Numerical and Analytical Methods in Geomechanics*, 39(6):618-634.
<https://doi.org/10.1002/nag.2329>
- Duan K, Kwok CY, Ma X, 2017. DEM simulations of sandstone under true triaxial compressive tests. *Acta Geotechnica*, 12(3):495-510.
<https://doi.org/10.1007/s11440-016-0480-6>
- Duan K, Ji YL, Wu W, et al., 2019a. Unloading-induced failure of brittle rock and implications for excavation-induced strain burst. *Tunnelling and Underground Space Technology*, 84:495-506.
<https://doi.org/10.1016/j.tust.2018.11.012>
- Duan K, Ji YL, Xu NW, et al., 2019b. Excavation-induced fault instability: possible causes and implications for seismicity. *Tunnelling and Underground Space Technology*, 92:103041.
<https://doi.org/10.1016/j.tust.2019.103041>
- Duriez J, Scholtès L, Donzé FV, 2016. Micromechanics of wing crack propagation for different flaw properties. *Engineering Fracture Mechanics*, 153:378-398.
<https://doi.org/10.1016/j.engfracmech.2015.12.034>
- Griffith AA, 1921. VI. The phenomena of rupture and flow in solids. *Philosophical Transactions of the Royal Society A: Mathematical, Physical and Engineering Sciences*, 221(582-593):163-198.
<https://doi.org/10.1098/rsta.1921.0006>
- He MC, Miao JL, Feng JL, 2010. Rock burst process of limestone and its acoustic emission characteristics under true-triaxial unloading conditions. *International Journal of Rock Mechanics and Mining Sciences*, 47(2):286-298.
<https://doi.org/10.1016/j.ijrmms.2009.09.003>
- Hoek E, Brown ET, 1980. *Underground Excavations in Rock*. Institute of Mining and Metallurgy, London, UK.
- Hoek E, Brown ET, 1997. Practical estimates of rock mass strength. *International Journal of Rock Mechanics and Mining Sciences*, 34(8):1165-1186.
[https://doi.org/10.1016/S1365-1609\(97\)80069-X](https://doi.org/10.1016/S1365-1609(97)80069-X)
- Huang CC, Yang WD, Duan K, et al., 2019. Mechanical behaviors of the brittle rock-like specimens with multi-non-persistent joints under uniaxial compression. *Construction and Building Materials*, 220:426-443.
<https://doi.org/10.1016/j.conbuildmat.2019.05.159>
- Itasca, 2008. PFC2D: Particle Flow Code in 2 Dimensions. Version 4.0, User's Manual. Itasca Consulting Group, Inc., Minneapolis, USA.
- Jiang RH, Duan K, Zhang QY, 2022. Effect of heterogeneity in micro-structure and micro-strength on the discrepancies between direct and indirect tensile tests on brittle rock. *Rock Mechanics and Rock Engineering*, 55(2):981-1000.
<https://doi.org/10.1007/s00603-021-02700-y>
- Kwok CY, Duan K, Pierce M, 2020. Modeling hydraulic fracturing in jointed shale formation with the use of fully coupled discrete element method. *Acta Geotechnica*, 15(1): 245-264.
<https://doi.org/10.1007/s11440-019-00858-y>
- Lajtai EZ, 1974. Brittle fracture in compression. *International Journal of Fracture*, 10(4):525-536.
<https://doi.org/10.1007/BF00155255>
- Li XB, Feng F, Li DY, et al., 2018. Failure characteristics of granite influenced by sample height-to-width ratios and intermediate principal stress under true-triaxial unloading conditions. *Rock Mechanics and Rock Engineering*, 51(5):1321-1345.
<https://doi.org/10.1007/s00603-018-1414-4>
- Li YP, Chen LZ, Wang YH, 2005. Experimental research on pre-cracked marble under compression. *International Journal of Solids and Structures*, 42(9-10):2505-2516.
<https://doi.org/10.1016/j.ijsolstr.2004.09.033>
- Malmgren L, Saiang D, Töyrä J, et al., 2007. The excavation

- disturbed zone (EDZ) at Kiirunavaara mine, Sweden—by seismic measurements. *Journal of Applied Geophysics*, 61(1):1-15.
<https://doi.org/10.1016/j.jappgeo.2006.04.004>
- Martin CD, 1997. Seventeenth Canadian geotechnical colloquium: the effect of cohesion loss and stress path on brittle rock strength. *Canadian Geotechnical Journal*, 34(5): 698-725.
<https://doi.org/10.1139/t97-030>
- Martin CD, Chandler NA, 1994. The progressive fracture of Lac du Bonnet granite. *International Journal of Rock Mechanics and Mining Sciences & Geomechanics Abstracts*, 31(6): 643-659.
[https://doi.org/10.1016/0148-9062\(94\)90005-1](https://doi.org/10.1016/0148-9062(94)90005-1)
- Mas Ivars D, Potyondy DO, Pierce M, et al., 2008. The smooth-joint contact model. The 8th World Congress on Computational Mechanics and 5th European Congress on Computational Methods in Applied Sciences and Engineering.
- Park CH, Bobet A, 2009. Crack coalescence in specimens with open and closed flaws: a comparison. *International Journal of Rock Mechanics and Mining Sciences*, 46(5): 819-829.
<https://doi.org/10.1016/j.ijrmms.2009.02.006>
- Potyondy DO, 2012. A flat-jointed bonded-particle material for hard rock. The 46th U.S. Rock Mechanics/Geomechanics Symposium, article ARMA-2012-501.
- Potyondy DO, Cundall PA, 2004. A bonded-particle model for rock. *International Journal of Rock Mechanics and Mining Sciences*, 41(8):1329-1364.
<https://doi.org/10.1016/j.ijrmms.2004.09.011>
- Tang CA, Kou SQ, 1998. Crack propagation and coalescence in brittle materials under compression. *Engineering Fracture Mechanics*, 61(3-4):311-324.
[https://doi.org/10.1016/S0013-7944\(98\)00067-8](https://doi.org/10.1016/S0013-7944(98)00067-8)
- Tapponnier P, Brace WF, 1976. Development of stress-induced microcracks in Westerly granite. *International Journal of Rock Mechanics and Mining Sciences & Geomechanics Abstracts*, 13(4):103-112.
[https://doi.org/10.1016/0148-9062\(76\)91937-9](https://doi.org/10.1016/0148-9062(76)91937-9)
- Wang YC, Mora P, 2008. Modeling wing crack extension: implications for the ingredients of discrete element model. *Pure and Applied Geophysics*, 165(3):609-620.
<https://doi.org/10.1007/s00024-008-0315-y>
- Wang YT, Zhou XP, Shou YD, 2017. The modeling of crack propagation and coalescence in rocks under uniaxial compression using the novel conjugated bond-based peridynamics. *International Journal of Mechanical Sciences*, 128-129:614-643.
<https://doi.org/10.1016/j.ijmecsci.2017.05.019>
- Wong LNY, Einstein HH, 2009. Systematic evaluation of cracking behavior in specimens containing single flaws under uniaxial compression. *International Journal of Rock Mechanics and Mining Sciences*, 46(2):239-249.
<https://doi.org/10.1016/j.ijrmms.2008.03.006>
- Yang SQ, Jing HW, 2011. Strength failure and crack coalescence behavior of brittle sandstone samples containing a single fissure under uniaxial compression. *International Journal of Fracture*, 168(2):227-250.
<https://doi.org/10.1007/s10704-010-9576-4>
- Yang SQ, Huang YH, Jing HW, et al., 2014. Discrete element modeling on fracture coalescence behavior of red sandstone containing two unparallel fissures under uniaxial compression. *Engineering Geology*, 178:28-48.
<https://doi.org/10.1016/j.enggeo.2014.06.005>
- Yang SQ, Tian WL, Huang YH, et al., 2016. An experimental and numerical study on cracking behavior of brittle sandstone containing two non-coplanar fissures under uniaxial compression. *Rock Mechanics and Rock Engineering*, 49(4):1497-1515.
<https://doi.org/10.1007/s00603-015-0838-3>
- Zhang JZ, Zhou XP, Zhu JY, et al., 2018. Quasi-static fracturing in double-flawed specimens under uniaxial loading: the role of strain rate. *International Journal of Fracture*, 211(1-2):75-102.
<https://doi.org/10.1007/s10704-018-0277-8>
- Zhang QY, Duan K, Jiao YY, et al., 2017. Physical model test and numerical simulation for the stability analysis of deep gas storage cavern group located in bedded rock salt formation. *International Journal of Rock Mechanics and Mining Sciences*, 94:43-54.
<https://doi.org/10.1016/j.ijrmms.2017.02.015>
- Zhang QY, Zhang Y, Duan K, et al., 2019. Large-scale geomechanical model tests for the stability assessment of deep underground complex under true-triaxial stress. *Tunnelling and Underground Space Technology*, 83:577-591.
<https://doi.org/10.1016/j.tust.2018.10.011>
- Zhang XP, Wong LNY, 2013. Loading rate effects on cracking behavior of flaw-contained specimens under uniaxial compression. *International Journal of Fracture*, 180(1): 93-110.
<https://doi.org/10.1007/s10704-012-9803-2>